

SUPPORTING INFORMATION

Local Electric Fields as a Natural Switch of Heme-Iron Protein Reactivity.

Daniel Bím,^a Anastassia N. Alexandrova^{a,b,}*

^a*Department of Chemistry and Biochemistry, University of California, Los Angeles, 607 Charles E. Young Drive East, Los Angeles, CA 90095-1569, USA*

^b*California NanoSystems Institute, University of California, Los Angeles, 570 Westwood Plaza, Los Angeles, California 90095-1569, USA*

Corresponding author:

*E-mail: ana@chem.ucla.edu

Supporting Information Contents

Computational Details	p. S2-S3
Supplementary Note S1: Failure of the DFT in the His-ligated peroxidase model	p. S4-S6
Supplementary Figures S1-S5.....	p. S7-S9
Supplementary Tables S1-S3	p. S10-S15
References.....	p. S16-S18

Geometry coordinates of the optimized structures as discussed in the main text are provided in a separate zip file.

COMPUTATIONAL DETAILS

Local Electric field analysis

For the statistical analysis of the local electric fields in the heme-iron proteins, we used a snapshot of the RCSB protein data bank¹ acquired on July 16, 2020, to identify all structures with the possible reactivity through the oxygenated Fe–O intermediate. To this point, we filtered the proteins in the RCSB protein data bank to heme-containing oxidoreductases (enzyme classification (EC) number starting with 1), and resolution lower than 2.5 Å. To remove redundancies, we kept only one structure with the same UniProtKB number.² The resulting ~200 proteins were subjected to several modifications to calculate the local electric fields:

- i) All ‘non-residue’ substances (e.g., waters, substrates, counterions, etc.) were removed,
- ii) The heme cofactor, Fe center, and the oxygen atom (bound to Fe) were removed,
- iii) The axial Fe-ligating residue (i.e., axial His, Cys, Tyr) was replaced with Ala.

For each of the proteins, we have assigned the atomic charges to each atom at the ‘EX-NPA_6-31Gd_PCM level’ as implemented in the web-based Atomic Charge Calculator³, and we calculated the electric field at the position of the original Fe atom using the Coulomb’s law:

$$\vec{E} = \frac{1}{4\pi\epsilon_0} \sum_i \frac{q_i \vec{r}_i}{r_i^2 r_i} \quad (1)$$

Density functional theory calculations

All of the calculations were carried out using the Turbomole 6.6 program.⁴ The structures were optimized using the TPSS functional⁵, the hybrid basis set (def2-TZVP for the Fe and all of the ligating atoms: O, N_{Por}, O/N/S_{Axial}; def2-SVP for the rest of the system)⁶, and the zero-damping dispersion correction (D3)⁷. The effect of solvation on geometry optimizations was included by employing the implicit conductor-like screening model (COSMO)⁸ with a dielectric constant of $\epsilon = 4$. The calculations were accelerated by resolution-of-identity approximation (RI).⁹

For the equilibrium geometries, the terms contributing to Gibbs free energy were calculated as follows:

$$G = E_{el} + G_{solv} + [E_{ZPVE} + RT - RT\ln Q], \quad (3)$$

where:

- i) E_{el} is the *in vacuo* electronic energy; calculated using RI-B3LYP-D3 method,¹⁰

- ii) G_{solv} is the free energy of solvation; calculated using the conductor-like screening model (COSMO),
- iii) $[E_{\text{ZPVE}} + RT - RT \ln Q]$ corresponds to the thermal enthalpic and entropic contributions to the solute energy with E_{ZPVE} and Q being the zero-point vibrational energy and the molecular partition function, respectively; obtained from frequency calculations with the rigid rotor/harmonic oscillator approximation (for $p = 1$ bar, $T = 298$ K), considering low-frequency vibration modes (≤ 100 cm $^{-1}$) to contribute to Q as hindered rotors.¹¹

The acid dissociation constants, one-electron reduction potentials, and proton-coupled electron-transfer potentials were evaluated as:

$$pK_A = [G_{\text{deprotonated}} - G_{\text{protonated}} + G_{\text{solv}}(\text{H}^+)] / (RT \cdot \ln(10)), \quad (4)$$

$$E^\circ = G_{\text{oxidized}} - G_{\text{reduced}} - E^\circ_{\text{abs}}(\text{reference}), \quad (5)$$

$$E^\circ_H = G_{\text{dehydrogenated}} - G_{\text{hydrogenated}} - E^\circ_{\text{abs}}(\text{reference}) + G_{\text{solv}}(\text{H}^+) \quad (6)$$

where G is the Gibbs free energy of the particular state of the solute (Eq. (3)), $G_{\text{solv}}(\text{H}^+)$ is the Gibbs free energy of solvation of proton, and $E^\circ_{\text{abs}}(\text{reference})$ is the absolute potential of a reference electrode. Note that we adopted the values of $G_{\text{solv}}(\text{H}^+) = -265.9$ kcal mol $^{-1}$ in water, and $E^\circ_{\text{abs}}(\text{reference}) = 4.28$ eV for standard hydrogen electrode in water.

The bond dissociation free energy (BDFE) for the O–H bond of the Fe^{IV}OH CpdII intermediate was calculated as:

$$\text{BDFE(O–H)} = 23.06 \times E^\circ_{\text{CpdII}} + 1.37 \times pK_{A,\text{CpdII}} + 57.6 \text{ kcal mol}^{-1} \quad (5)$$

The effect of the external electric field was evaluated only to the $E_{\text{el}} + G_{\text{solv}}$ terms, while the thermal contributions (i.e., frequency calculations) were neglected. The external electric field as implemented in the Turbomole 6.6 was always oriented parallel with the Fe–O bond with the magnitude varying from -0.01 a.u. ($= -51.42$ MV cm $^{-1}$) to $+0.01$ a.u. ($= +51.42$ MV cm $^{-1}$).

SUPPLEMENTARY NOTE S1: Failure of the DFT in the His-ligated peroxidase model

As demonstrated in **Figure 8** in the main text, the description of the physicochemical properties (such as E°_{CpdI} and $pK_{\text{A,CpdII}}$) is unphysical in the negative F_z region of the applied OEEF using the DFT methodology. The most evident failure is observed for the His-ligated system, which suggests that problems arise from the problematic description of the near degeneracy of the π_{Trp} and Por a_{1u}/a_{2u} orbitals. Note that since the CpdI intermediate is described as the doublet spin state with the ferromagnetically-coupled triplet spin state on the ‘Fe–O’ and the unpaired radical that is delocalized between Por and Trp fragments, this suggests that Por and Trp orbitals should be as well close in energy in the reduced $\text{Fe}^{\text{IV}}\text{O}$ CpdII state with both orbitals doubly occupied. From the evolution of the Por a_{1u} and π_{Trp} orbital energies in the $\text{Fe}^{\text{IV}}\text{O}$ CpdII intermediate with the change of the OEEF in the F_z direction (see **Figure 9** in the main text), it is clear that such a description is correctly predicted by DFT in the zero field, where the Por a_{1u} and π_{Trp} orbitals are indeed degenerate. However, the π_{Trp} energy change appears to be overestimated as a response to the OEEF. Consequently, the π_{Trp} (HOMO) becomes erroneously destabilized in the negative field, leading to a large increase in the HOMO orbital energy and thus an artificially small E°_{CpdI} . This is likely an effect of the incorrect description of the charge delocalization using DFT methodology or improper description of the near-degenerate orbitals with the single determinant.

To clarify the origin of the error, we have introduced multiple modifications to our computational protocol to rule out the effect of the choice of the functional, basis set, surrounding environment, etc. In detail, we can conclude that the $\text{Fe}^{\text{IV}}\text{O}$ CpdII state is improperly described in the negative fields, and E°_{CpdI} erroneous description does not change, when the following modifications are introduced:

- (i) hybrid (B3LYP) vs. pure (TPSS) functional,
- (ii) larger basis set (def2-TZVP on all atoms),
- (iii) gas-phase vs. COSMO-embedded calculations,
- (iv) single-point calculations vs. structure optimizations at different OEEF,
- (v) embedding the model in the point charges instead of using OEEF,
- (vi) calculations with and without the resolution-of-identity approximation,
- (vii) increased grid size (m^3 vs. m^4).

To also eliminate the possibility that different spin states are followed in the zero (positive) field and the negative field region, we have analyzed the orbitals evolution (e.g., shape and

energies) and the Mulliken spin densities along the OEEF coordinate. Both were found to respond linearly to the applied field in positive and negative directions. We have also performed calculations at different (higher-lying) spin states, e.g., unrestricted and restricted singlet and quintet, demonstrating no spin state crossing in the evaluated OEEF region or a different behavior of the Fe^{IV}O CpdII energy.

Finally, the behavior is somewhat remedied using the simplified (truncated) model system, excluding the Asp and Trp residues H-bonded to axial His ligand. By this, we force the electronic configuration, i.e., unpaired radical in CpdI or HOMO orbital in Fe^{IV}O CpdII, to be situated at the Por fragment. As illustrated in **Figure S2**, all three states of interest are now close in energy, and their progression in the OEEF is similar. However, the increase in energy in the positive field region (**Figure S2, left**) and increase in $pK_{A,CpdII}$ with the increased F_z (**Figure S2, right**) are rather unexpected, and since this is not observed in either Tyr- or Cys-ligated models, we consider this to be an artifact originating from the incomplete representation of the model system. As one example of the simplification, we note that in Tyr- and Cys- models, the electron density in CpdI intermediate is preferably located on the axial ligand with only partial electron density situated on the Por fragment (*cf.* **Table 2** in the main text). However, such electron configuration is not observed in the His-ligated truncated model (without Asp and Trp residues), where the spin density is 0.02 e on His and 1.1 e on Por. The absence of the Trp residue thus clearly affects the possibility of the electron delocalization in the system.

Multiconfiguration self-consistent field (MCSCF) calculations

To further examine the origin of the error in the Fe^{IV}O CpdII state energy progression at the negative F_z , we have performed the MCSCF calculations. As implemented in the MOLCAS 8.4 program,^{12–15} multiconfigurational/multireference approximations to wave function theory: CASSCF^{16,17} and MC-PDFT^{18,19} methods were applied in combination with the ANO-RCC^{20,21} basis set to size-reduced DFT-equilibrated model of the peroxidase enzyme (*cf.* **Figure S3**). The ANO-RCC basis set, contracted to [6s5p3d2f1g] for Fe, [4s3p2d] for N and O atoms, [3s2p] for C atoms, and [2s] for H atoms, was used. The second-order Douglas–Kroll–Hess (DKH2)^{22–24} one-electron spin-less Hamiltonian was applied for all WFT-based calculations to allow for spin-free relativistic effects. The Cholesky decomposition technique²⁵ with a threshold of 10^{-6} a.u. was used to approximate two-electron integrals. Complete active space used in CASSCF calculations is

specified in **Figure S4** and comprises 18 electrons in 15 orbitals (denoted as 18e,15o). The selection of the active orbitals was inspired by ref. 26, and expanded to include additional orbitals from **Figure S4**. Note that due to the absence of the dynamic correlation in the CASSCF, some states of interest might be described as high-energy excited states, providing a qualitatively incorrect character of the CASSCF solution.²⁶ Therefore, we have performed the state-averaged (SA)-CASSCF (average of the 5 lowest states with the equal weights) to cover the main states for each irrep and multiplicity, followed by the on-top MC-PDFT correction at the tBLYP level.

In **Figure S5**, the results of CASSCF and MC-PDFT calculations are compared with the DFT (B3LYP) method. Interestingly, the multiconfiguration methods exhibit the equivalent behavior and were not able to resolve the problem. Since further examination goes far beyond the scope of the article, we may only speculate that the problem persists due to an insufficient active space with 18 electrons and 15 orbitals. For example, it was previously presented that metal double-d shell orbitals are required for the proper energetics.²⁸

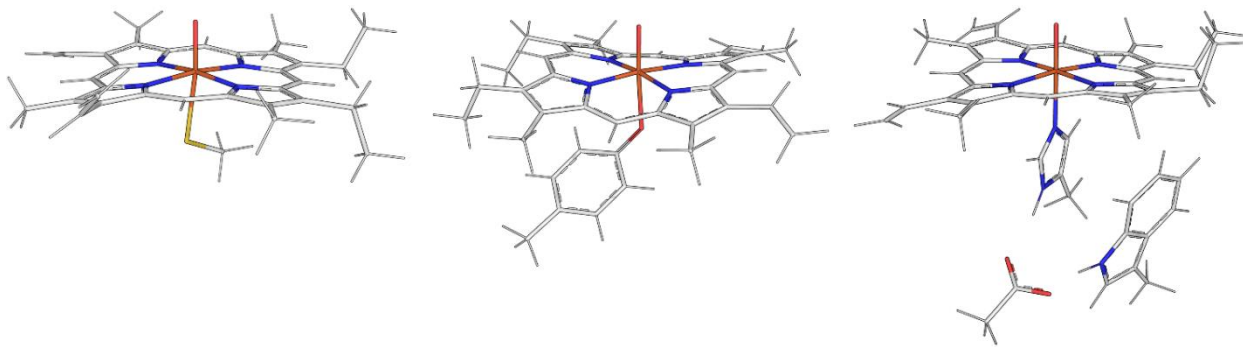


Figure S1. Computational cluster models truncated from the crystal structures deposited in the RCSB protein data bank with the PDB codes: 1dz9 (P450cam; *left*), 1mqf (*P. mirabilis* catalase; *middle*), and 5jqr (APX; *right*).

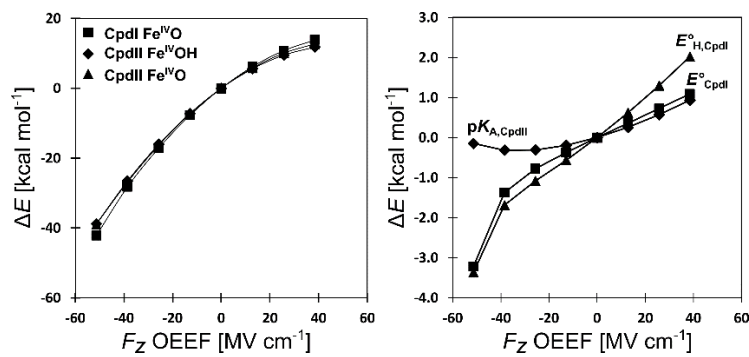


Figure S2. Left: Relative change in the energy of the individual states from [Scheme 2](#) with the variation of the OEEF F_z in the truncated His-ligated model, excluding the Asp and Trp residues. Right: Progression of the physicochemical properties from [Scheme 2](#) in the main text in the truncated His-ligated model, excluding the Asp and Trp residues.

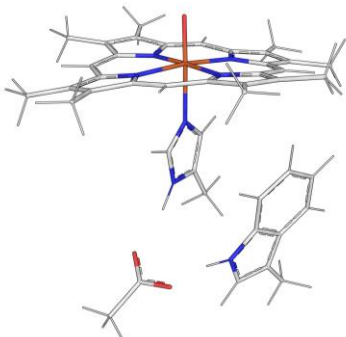


Figure S3. Truncated model of the His-ligated peroxidase system, utilized in the multiconfiguration calculations at the CASSCF and MC-PDFT/CASSCF level.

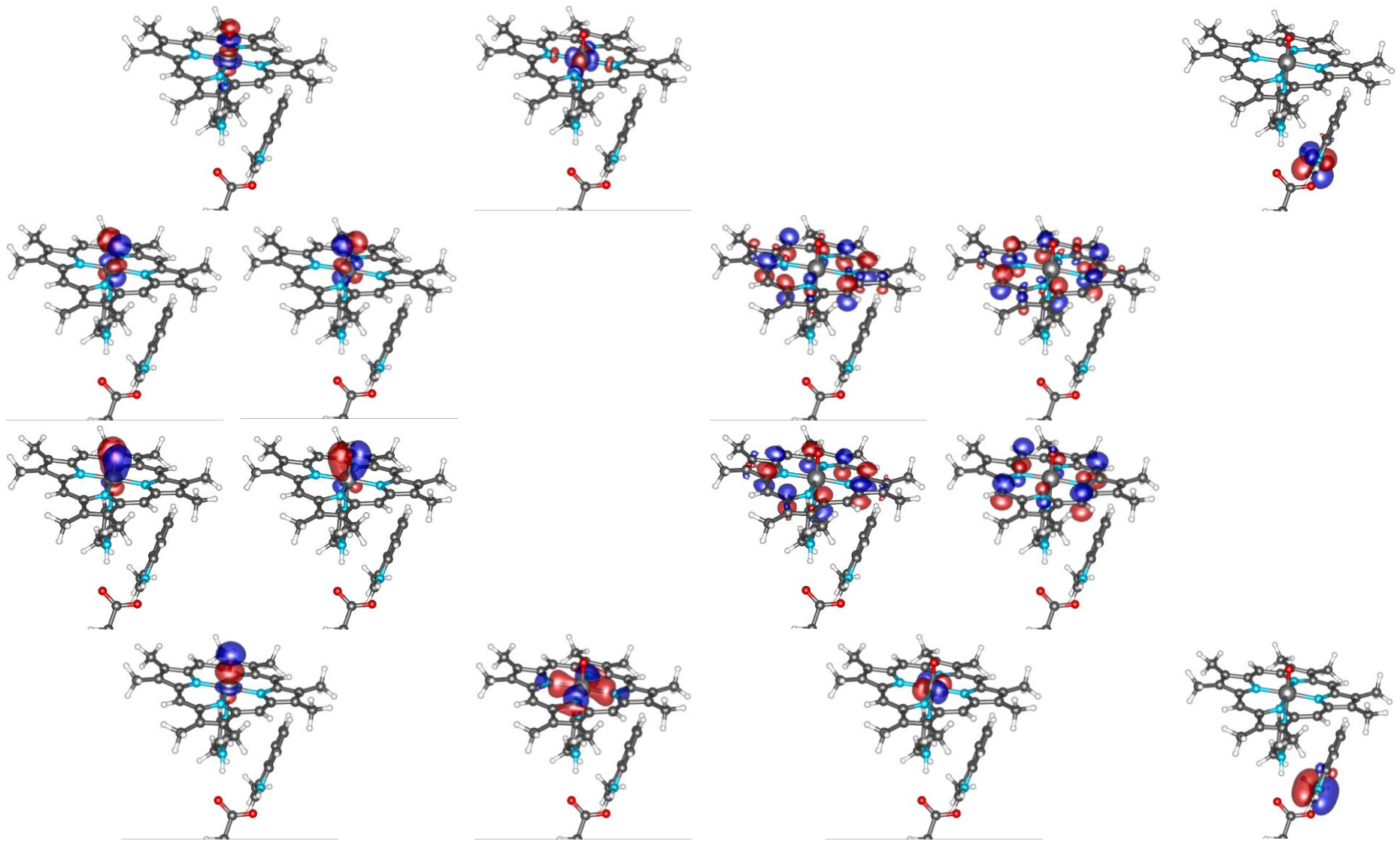


Figure S4. Molecular-orbital diagram given for the His-ligated peroxidase model. The complete active space consists of 18 electrons in 15 orbitals.

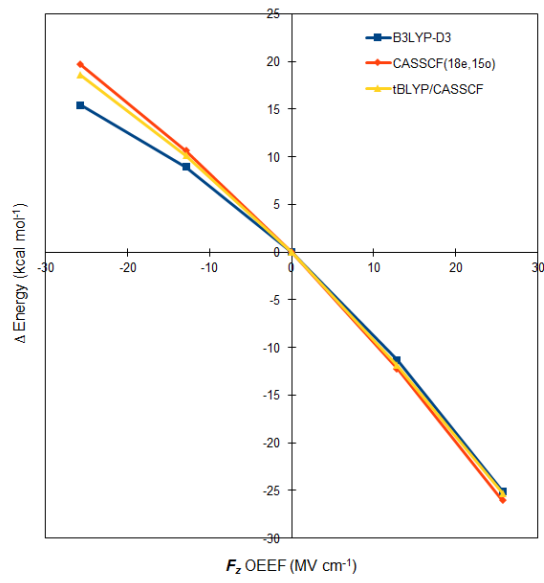


Figure S5. Relative change in the energy of the Fe^{IV}O CpdII state of the His-ligated model with the variation of the OEEF F_z .

Table S1: The F_x , F_y , and F_z components of the LEF vector for each of the proteins in the whole series of the heme-iron oxidoreductases.

PDB code	F_x	F_y	F_z	EC number	Axial ligand
1a4e	-3.6	-15.1	1.4	1.11.1.6	Y
1apx	-27.0	-0.6	-21.5	1.11.1.11	H
1bgp	-26.2	14.3	-11.5	1.11.1.7	H
1dgh	-22.1	-11.7	7.4	1.11.1.6	Y
1dz9	-5.2	-0.3	25.2	1.14.15.1	C
1ebe	-22.1	-4.9	-26.7	1.11.1.5	H
1gvh	-6.4	2.1	-18.1	1.6.99.7	H
1gwf	-11.0	-17.9	-4.1	1.11.1.6	Y
1gwh	-10.5	-15.7	10.1	1.11.1.6	Y
1hch	-5.5	-9.4	-36.6	1.11.1.7	H
1iyn	-15.8	-4.1	-25.8	1.11.1.11	H
1jio	-7.7	4.8	28.1	1	C
1lga	-1.4	2.2	-5.8	1.11.1	H
1ly9	-6.2	-0.9	-6.3	1.11.1.7	H
1m7s	9.5	16.0	-1.0	1.11.1.6	Y
1mjt	14.3	23.6	34.1	1.14.13.39	C
1mqf	-11.1	-9.1	8.6	1.11.1.6	Y
1n6b	-26.6	15.5	33.1	1.14.14.1	C
1p3v	17.3	11.1	-0.7	1.14.99.3	H
1pa2	-14.0	2.9	-23.9	1.11.1.7	H
1qgj	-17.0	5.2	-23.8	1.11.1	H
1qpa	-1.6	4.6	-6.3	1.11.1	H
1si8	-23.8	-9.5	5.3	1.11.1.6	Y
1sj2	-18.4	-10.9	-11.6	1.11.1.6	H
1sy7	5.0	16.0	1.1	1.11.1.6	Y
1u5u	23.5	1.0	1.4	4.2.1.92	Y
1ued	-18.2	2.9	50.3	1.14	C
1ulw	11.5	6.0	42.4	1.7.99.7	C
1v8x	-11.9	-2.5	-18.7	1.14.99.3	H
1wox	-8.0	-4.9	-3.5	1.14.99.3	H
2a9e	-21.3	-10.5	1.7	1.11.1.6	Y
2d09	-9.4	8.3	25.7	1.14	C
2e39	-3.9	-1.1	-2.1	1.11.1.7	H
2hi4	-1.4	-0.7	12.9	1.14.14.1	C
2iqf	-20.0	-9.7	2.5	1.11.1.6	Y
2j2m	12.9	12.5	1.9	1.11.1.6	Y
2nnj	-35.5	22.6	38.3	1.14.14.1	C
2ve3	3.1	3.6	13.7	1.14	C

2vxh	16.1	13.8	-12.4	1.13.11.49	H
2w0a	-3.5	0.1	20.1	1.14.13.70	C
2wh8	-14.4	10.2	44.0	1.14	C
2wm4	1.3	13.7	13.4	1.14	C
2x5l	-20.3	29.0	41.4	1.14	C
2xkr	-26.8	18.6	42.5	1.14	C
2yp1	22.0	-7.3	32.1	1.11.2.1	C
2z3t	-2.0	-2.7	17.7	1	C
2zdo	3.9	0.9	-36.0	1.14.99.3	H
2zqx	-4.1	13.0	23.6	1.14	C
3aba	0.4	8.3	8.2	1.14.13	C
3abb	-12.8	26.6	42.5	1.14.13	C
3atj	-14.0	-3.5	-18.2	1.11.1.7	H
3b4x	-25.8	16.3	22.9	1.14.14.1	C
3bk9	1.0	-8.5	16.6	1.13.11.11	H
3cv8	5.3	2.2	7.7	1.14.14.1	C
3czh	-12.7	16.1	14.9	1.14.14	C
3czy	6.0	3.7	6.5	1.14.99.3	H
3e65	11.4	27.6	40.2	1.14.13.39	C
3gas	-4.4	7.1	-5.0	1.14.99.3	H
3hb6	-8.7	-9.6	6.7	1.11.1.6	Y
3hdl	-12.8	5.2	-25.4	1.11.1	H
3lgm	1.8	8.0	-37.1	1.14.99.3	H
3m8m	-13.1	-5.9	-10.2	1.11.1.13	H
3mdr	-27.7	25.1	28.7	1.14.13.98	C
3mgx	-30.7	22.1	56.3	1.14.14.1	C
3mvr	-26.6	26.9	43.4	1.14.14.1	C
3n9y	-5.6	-1.5	19.6	1.14.15.6	C
3nn1	9.5	-3.7	-16.2	1.13.11.49	H
3ozv	-6.8	-2.0	-4.3	1.14.12.17	H
3qpi	8.1	0.7	-15.8	1.13.11.49	H
3r9b	-0.2	3.0	3.7	1.14	C
3re8	-24.8	-13.5	-2.1	1.11.1.6	Y
3riv	-11.5	-9.7	-15.5	1.11.1.11	H
3rke	-15.1	-23.1	12.4	1.11.1.7	H
3rqo	2.6	20.4	33.6	1.14.13.39	C
3rw1	-16.4	16.6	42.7	1.14.15.3	C
3s4f	-19.7	-23.8	8.5	1.11.1.7	H
3t3q	-11.3	6.2	15.7	1.14.14.1	C
3t3z	-23.3	19.9	21.0	1.14.13	C
3ut2	-12.9	-9.2	-11.5	1.11.1.21	H

3uw8	-25.0	-13.0	-8.5	1.11.1.21	H
3v8d	-19.5	14.6	55.8	1.14.13.17	C
3vm4	0.0	-0.3	19.9	1.11.2.4	C
3vxi	25.1	-16.0	17.3	1.11.1.19	H
3wrh	7.8	-5.8	18.8	1.14.15.1	C
3wsp	6.8	4.7	17.0	1.14.14.1	C
3wxo	-23.1	-2.3	-24.2	1.11.1.21	H
3zj5	6.5	18.2	-1.6	1.11.1.6	Y
3zkp	-16.6	22.7	44.4	1.14.13.154	C
4a5g	-15.3	-4.0	-21.3	1.11.1.7	H
4au9	11.8	-12.2	-10.2	1.11.1.19	H
4aul	19.8	18.9	14.9	1.11.1.6	Y
4b2y	3.9	20.6	2.9	1.11.1.6	Y
4b7f	-9.1	-18.4	-0.8	1.11.1.6	Y
4ccp	-13.7	-7.3	-18.4	1.11.1.5	H
4coh	1.2	1.3	20.5	1.14.13.70	C
4cuo	-12.8	-0.5	-20.6	1.11.1.7	H
4d1o	11.9	29.7	38.8	1.14.13.39	C
4d3t	8.7	26.2	41.4	1.14.13.165	C
4d6z	0.2	6.0	24.3	1.14.13.157	C
4dnj	-11.1	2.5	10.4	1.14	C
4e2p	-9.2	35.0	50.7	1.13.12	C
4eji	-13.2	2.9	17.3	1.14.14.1	C
4ep6	-3.4	-7.3	18.9	1	C
4g2c	11.7	-17.9	-4.2	1	H
4g3j	-5.2	4.5	23.4	1.14.13.70	C
4g7t	-4.9	-1.7	-1.3	1.14.99.3	H
4ggv	-4.5	7.5	55.4	1.14.13	C
4gqe	16.0	26.9	37.0	1.14.13.39	C
4grc	31.1	0.9	17.9	1.11.1.19	H
4gs1	27.3	3.4	9.5	1.11.1.19	H
4gt2	31.1	1.5	6.8	1.11.1.19	H
4hov	10.8	-6.2	-25.8	1.11.1	H
4hsw	-13.0	-16.9	-6.8	1.11.1.7	H
4i91	-8.5	6.5	5.8	1.14.13	C
4ict	-4.3	7.1	21.5	1.14	C
4jm5	-12.7	-11.6	-35.7	1.11.1.5	H
4l0f	-20.6	18.2	58.2	1.14	C
4lht	1.0	5.5	25.1	1.14	C
4lxj	-18.9	0.1	47.1	1.14.13.70	C
4nl5	5.2	-5.3	-26.3	1.14.99.3	H

4nos	17.2	25.5	33.8	1.14.13.39	C
4nz2	-29.7	21.5	38.2	1.14.13	C
4o1z	-18.0	-24.1	6.2	1.14.99.1	H
4ph9	-16.5	-29.4	0.5	1.14.99.1	H
4rm4	-11.7	27.3	39.2	1.14	C
4tt5	-12.8	5.4	22.9	1.14	C
4tvf	-13.6	17.8	33.2	1.14.14.1	C
4u72	-3.2	-1.7	7.6	1.13.11.52	H
4ubs	-5.6	3.9	3.3	1.14.15.11	C
4uh1	2.2	-3.3	16.5	1.14.13.70	C
4wnu	-14.6	13.0	30.9	1.14.14.1	C
4xmc	10.6	4.1	-8.5	1.7.6.1	H
4y55	-12.0	-22.2	15.7	1.11.1.7	H
4yt3	-10.1	12.5	44.1	1.14.99	C
4yzr	0.5	9.7	6.2	1.14	C
5a12	14.8	-1.5	-28.5	1.13.11.49	H
5a13	6.7	-3.5	-31.5	1.13.11.49	H
5aog	-20.6	12.1	-18.1	1.11.1.7	H
5dqn	-15.1	26.3	37.1	1.14.13.151	C
5edt	0.7	6.7	27.2	1.14	C
5esn	-13.7	2.8	45.9	1.14.13.70	C
5fiw	-9.1	-30.6	28.4	1.11.2.2	H
5foi	-6.8	6.7	5.8	1.14	C
5fuk	15.7	-21.7	29.5	1.11.2.1	C
5fw4	22.5	-1.6	12.0	1.11.1.19	H
5gnl	-20.9	18.1	26.3	1.14.15.15	C
5gt2	28.3	0.4	21.4	1.11.1	H
5hdi	-14.8	18.3	51.0	1.14	C
5hiw	-18.0	10.0	51.2	1.14	C
5hwz	8.8	2.2	-14.1	1.7.6.1	H
5it1	-17.2	10.8	43.2	1.14.14.1	C
5jlc	-18.5	1.3	42.1	1.14.13.70	C
5jqr	-4.4	9.0	4.1	1.11.1.11	H
5kq3	-20.4	-15.4	-18.5	1.11.1.21	H
5kzl	-2.0	3.5	2.6	1.14.14.18	H
5l1s	-17.3	23.2	29.2	1.14.19.8	C
5l92	0.3	3.6	8.6	1.14.14	C
5lie	6.4	12.5	15.9	1.14	C
5o11	3.3	-5.5	16.5	1.13	H
5o4k	-1.8	5.1	20.0	1.14.21.9	C
5sx0	-17.5	-9.2	-15.0	1.11.1.21	H

5tia	-11.3	-13.6	3.9	1.13.11.11	H
5tz1	-1.7	-6.8	21.3	1.14.13.70	C
5uo7	16.7	28.6	42.5	1.14.13.39	C
5wp2	-2.5	5.4	21.4	1.14.21.9	C
5yem	9.4	13.9	1.5	1.11.1.6	Y
5ylw	-7.9	13.3	41.3	1.14.13.190	C
6a17	-15.4	0.6	19.4	1.14	C
6b11	-7.8	3.8	9.4	1.14.13.186	C
6cr2	5.8	-4.8	20.0	1.14.13.70	C
6fyi	3.7	-4.1	4.8	1.11.1	H
6fyj	-3.2	-1.2	15.7	1.11.2.4	C
6g5o	-18.2	5.6	39.9	1.14.15	C
6gk5	-12.0	6.3	6.3	1.14	C
6h11	-18.9	19.3	30.3	1.14.14.1	C
6h1t	-12.4	22.4	27.7	1.14.14.1	C
6iss	-1.4	5.1	-8.8	1.11.1.14	H
6j95	-1.3	26.1	13.8	1.14	C
6l8h	-12.6	35.3	36.5	1.14.14.158	C
6mcw	-13.5	4.7	34.2	1.14.13.70	C
6mjm	-5.5	17.0	31.6	1.14.14.1	C
6mq0	-20.1	-9.4	-11.8	1.11.1.21	H
6nsw	12.3	19.7	-1.3	1.11.1.6	Y
6rjn	-11.5	-7.3	0.6	1.11.1.6	Y
6rjr	-6.0	-11.8	8.2	1.11.1.6	Y
6tb8	35.6	8.4	29.6	1.11.1	H
6u30	-0.4	-1.0	2.9	1.14	C
6wk3	2.7	-3.9	-21.3	1.14.12.17	H

Table S2: The average absolute $|F_x|$, $|F_y|$, and $|F_z|$ components of the LEF vector for the heme-iron oxidoreductases grouped according to their EC numbers.

EC Number	Avg. $ F_x $	Avg. $ F_y $	Avg. $ F_z $	Std. dev. $ F_x $	Std. dev. $ F_y $	Std. dev. $ F_z $
1	12.1	10.7	20.6	8.2	8.6	14.5
1.7	10.3	4.1	21.7	1.4	1.9	18.2
1.11	14.7	9.7	12.8	8.3	6.5	9.5
1.11.1	15.0	9.8	12.1	8.2	6.3	9.2
1.11.1.5	16.1	7.9	26.9	5.2	3.4	8.7
1.11.1.6	12.8	13.9	4.4	6.7	3.9	4.1
1.11.1.7	13.7	10.4	15.5	6.3	9.0	9.1
1.11.1.11	14.7	5.8	16.7	9.5	4.3	9.4
1.11.1.19	24.8	5.9	12.3	7.2	6.5	4.4
1.11.1.21	19.8	9.8	14.9	4.3	4.4	5.7
1.11.2	10.2	7.6	24.3	10.4	9.9	7.8
1.13	8.3	8.7	20.0	5.0	10.4	13.6
1.14	11.0	11.9	26.2	8.1	9.4	15.3
1.14.13	11.5	14.2	32.4	7.9	10.6	13.2
1.14.14	14.7	14.0	26.2	10.1	9.5	14.0
1.14.15	11.4	7.4	25.1	6.8	7.1	13.4
1.14.99	9.0	9.3	15.5	5.7	9.0	16.2

Table S3: The average absolute $|F_x|$, $|F_y|$, and $|F_z|$ components of the LEF vector for the heme-iron oxidoreductases grouped according to their axial ligands.

Axial ligand	Avg. $ F_x $	Avg. $ F_y $	Avg. $ F_z $	Std. dev. $ F_x $	Std. dev. $ F_y $	Std. dev. $ F_z $
Cys	11.3	12.3	28.5	8.3	9.6	14.1
His	13.1	7.4	15.0	8.4	6.6	9.5
Tyr	13.0	13.5	4.0	6.9	4.8	3.8

REFERENCES

- (1) Berman, H. M.; Westbrook, J.; Feng, Z.; Gilliland, G.; Bhat, T. N.; Weissig, H.; Shindyalov, I. N.; Bourne, P. E. The Protein Data Bank. *Nucleic Acids Res.* **2000**, *28* (1), 235–242. <https://doi.org/10.1093/nar/28.1.235>.
- (2) Consortium, T. U. UniProt: A Worldwide Hub of Protein Knowledge. *Nucleic Acids Res.* **2019**, *47* (D1), D506–D515. <https://doi.org/10.1093/nar/gky1049>.
- (3) Ionescu, C.-M.; Sehnal, D.; Falginella, F. L.; Pant, P.; Pravda, L.; Bouchal, T.; Svobodová Vařeková, R.; Geidl, S.; Koča, J. AtomicChargeCalculator: Interactive Web-Based Calculation of Atomic Charges in Large Biomolecular Complexes and Drug-like Molecules. *J. Cheminform.* **2015**, *7* (1), 50. <https://doi.org/10.1186/s13321-015-0099-x>.
- (4) Ahlrichs, R.; Bär, M.; Häser, M.; Horn, H.; Kölmel, C. Electronic Structure Calculations on Workstation Computers: The Program System Turbomole. *Chem. Phys. Lett.* **1989**, *162* (3), 165–169. [https://doi.org/10.1016/0009-2614\(89\)85118-8](https://doi.org/10.1016/0009-2614(89)85118-8).
- (5) Tao, J.; Perdew, J. P.; Staroverov, V. N.; Scuseria, G. E. Climbing the Density Functional Ladder: Nonempirical Meta--Generalized Gradient Approximation Designed for Molecules and Solids. *Phys. Rev. Lett.* **2003**, *91* (14), 146401. <https://doi.org/10.1103/PhysRevLett.91.146401>.
- (6) Weigend, F.; Ahlrichs, R. Balanced Basis Sets of Split Valence, Triple Zeta Valence and Quadruple Zeta Valence Quality for H to Rn: Design and Assessment of Accuracy. *Phys. Chem. Chem. Phys.* **2005**, *7* (18), 3297–3305. <https://doi.org/10.1039/b508541a>.
- (7) Grimme, S.; Antony, J.; Ehrlich, S.; Krieg, H. A Consistent and Accurate Ab Initio Parametrization of Density Functional Dispersion Correction (DFT-D) for the 94 Elements H-Pu. *J. Chem. Phys.* **2010**, *132* (15). <https://doi.org/10.1063/1.3382344>.
- (8) Klamt, A.; Schüürmann, G. COSMO: A New Approach to Dielectric Screening in Solvents with Explicit Expressions for the Screening Energy and Its Gradient. *J. Chem. Soc. Perkin Trans. 2* **1993**, No. 5, 799–805. <https://doi.org/10.1039/P29930000799>.
- (9) Eickorn, K.; Treutler, O.; Öhm, H.; Häser, M.; Ahlrichs, R. Auxiliary Basis Sets to Approximate Coulomb Potentials. *Chem. Phys. Lett.* **1995**, *240* (4), 283–290. [https://doi.org/10.1016/0009-2614\(95\)00621-A](https://doi.org/10.1016/0009-2614(95)00621-A).
- (10) Becke, A. D. Density-functional Thermochemistry. III. The Role of Exact Exchange. *J. Chem. Phys.* **1993**, *98* (7), 5648–5652. <https://doi.org/10.1063/1.464913>.

- (11) Grimme, S. Supramolecular Binding Thermodynamics by Dispersion-Corrected Density Functional Theory. *Chem. - A Eur. J.* **2012**, *18* (32), 9955–9964. <https://doi.org/10.1002/chem.201200497>.
- (12) Aquilante, F.; De Vico, L.; Ferré, N.; Ghigo, G.; Malmqvist, P.-åke; Neogrády, P.; Pedersen, T. B.; Pitoňák, M.; Reiher, M.; Roos, B. O.; et al. MOLCAS 7: The Next Generation. *J. Comput. Chem.* **2010**, *31* (1), 224–247. [https://doi.org/https://doi.org/10.1002/jcc.21318](https://doi.org/10.1002/jcc.21318).
- (13) Aquilante, F.; Autschbach, J.; Carlson, R. K.; Chibotaru, L. F.; Delcey, M. G.; De Vico, L.; Fdez. Galván, I.; Ferré, N.; Frutos, L. M.; Gagliardi, L.; et al. Molcas 8: New Capabilities for Multiconfigurational Quantum Chemical Calculations across the Periodic Table. *J. Comput. Chem.* **2016**, *37* (5), 506–541. <https://doi.org/https://doi.org/10.1002/jcc.24221>.
- (14) Veryazov, V.; Widmark, P.-O.; Serrano-Andrés, L.; Lindh, R.; Roos, B. O. 2MOLCAS as a Development Platform for Quantum Chemistry Software. *Int. J. Quantum Chem.* **2004**, *100* (4), 626–635. <https://doi.org/https://doi.org/10.1002/qua.20166>.
- (15) Karlström, G.; Lindh, R.; Malmqvist, P.-Å.; Roos, B. O.; Ryde, U.; Veryazov, V.; Widmark, P.-O.; Cossi, M.; Schimmelpfennig, B.; Neogrady, P.; et al. MOLCAS: A Program Package for Computational Chemistry. *Comput. Mater. Sci.* **2003**, *28* (2), 222–239. [https://doi.org/https://doi.org/10.1016/S0927-0256\(03\)00109-5](https://doi.org/https://doi.org/10.1016/S0927-0256(03)00109-5).
- (16) Siegbahn, P. E. M.; Almlöf, J.; Heiberg, A.; Roos, B. O. The Complete Active Space SCF (CASSCF) Method in a Newton–Raphson Formulation with Application to the HNO Molecule. *J. Chem. Phys.* **1981**, *74* (4), 2384–2396. <https://doi.org/10.1063/1.441359>.
- (17) Roos, B. O.; Taylor, P. R.; Sigbahn, P. E. M. A Complete Active Space SCF Method (CASSCF) Using a Density Matrix Formulated Super-CI Approach. *Chem. Phys.* **1980**, *48* (2), 157–173. [https://doi.org/https://doi.org/10.1016/0301-0104\(80\)80045-0](https://doi.org/https://doi.org/10.1016/0301-0104(80)80045-0).
- (18) Carlson, R. K.; Li Manni, G.; Sonnenberger, A. L.; Truhlar, D. G.; Gagliardi, L. Multiconfiguration Pair-Density Functional Theory: Barrier Heights and Main Group and Transition Metal Energetics. *J. Chem. Theory Comput.* **2015**, *11* (1), 82–90. <https://doi.org/10.1021/ct5008235>.
- (19) Li Manni, G.; Carlson, R. K.; Luo, S.; Ma, D.; Olsen, J.; Truhlar, D. G.; Gagliardi, L. Multiconfiguration Pair-Density Functional Theory. *J. Chem. Theory Comput.* **2014**, *10* (9), 3669–3680. <https://doi.org/10.1021/ct500483t>.

- (20) Widmark, P.-O.; Malmqvist, P.-Å.; Roos, B. O. Density Matrix Averaged Atomic Natural Orbital (ANO) Basis Sets for Correlated Molecular Wave Functions. *Theor. Chim. Acta* **1990**, *77* (5), 291–306. <https://doi.org/10.1007/BF01120130>.
- (21) Roos, B. O.; Lindh, R.; Malmqvist, P.-Å.; Veryazov, V.; Widmark, P.-O. New Relativistic ANO Basis Sets for Transition Metal Atoms. *J. Phys. Chem. A* **2005**, *109* (29), 6575–6579. <https://doi.org/10.1021/jp0581126>.
- (22) Douglas, M.; Kroll, N. M. Quantum Electrodynamical Corrections to the Fine Structure of Helium. *Ann. Phys. (N. Y.)* **1974**, *82* (1), 89–155. [https://doi.org/10.1016/0003-4916\(74\)90333-9](https://doi.org/10.1016/0003-4916(74)90333-9).
- (23) Hess, B. A. Relativistic Electronic-Structure Calculations Employing a Two-Component No-Pair Formalism with External-Field Projection Operators. *Phys. Rev. A* **1986**, *33* (6), 3742–3748. <https://doi.org/10.1103/PhysRevA.33.3742>.
- (24) Jansen, G.; Hess, B. A. Revision of the Douglas-Kroll Transformation. *Phys. Rev. A* **1989**, *39* (11), 6016–6017. <https://doi.org/10.1103/PhysRevA.39.6016>.
- (25) Aquilante, F.; Malmqvist, P.-Å.; Pedersen, T. B.; Ghosh, A.; Roos, B. O. Cholesky Decomposition-Based Multiconfiguration Second-Order Perturbation Theory (CD-CASPT2): Application to the Spin-State Energetics of CoIII(Diiminato)(NPh). *J. Chem. Theory Comput.* **2008**, *4* (5), 694–702. <https://doi.org/10.1021/ct700263h>.
- (26) Radoń, M.; Broclawik, E. Peculiarities of the Electronic Structure of Cytochrome P450 Compound I: CASPT2 and DFT Modeling. *J. Chem. Theory Comput.* **2007**, *3* (3), 728–734. <https://doi.org/10.1021/ct600363a>.
- (27) Bao, J. L.; Wang, Y.; He, X.; Gagliardi, L.; Truhlar, D. G. Multiconfiguration Pair-Density Functional Theory Is Free From Delocalization Error. *J. Phys. Chem. Lett.* **2017**, *8* (22), 5616–5620. <https://doi.org/10.1021/acs.jpclett.7b02705>.
- (28) PIERLOOT, K. The CASPT2 Method in Inorganic Electronic Spectroscopy: From Ionic Transition Metal to Covalent Actinide Complexes*. *Mol. Phys.* **2003**, *101* (13), 2083–2094. <https://doi.org/10.1080/0026897031000109356>.